

# Electromagnetic Resonances of Individual Single-Walled Carbon Nanotubes With Realistic Shapes: A Characteristic Modes Approach

Ahmed M. Hassan, *Member, IEEE*, Fernando Vargas-Lara, Jack F. Douglas, and Edward J. Garboczi

**Abstract**—In composites, carbon nanotubes (CNTs) are rarely perfectly straight and they usually exhibit complex shapes. In this paper, we employ the method-of-moments formulation for arbitrary thin wires to study the electromagnetic scattering characteristics of CNTs with realistic shapes. More than 800 different CNT shapes were simulated in this work. These shapes were generated using a coarse-grained molecular dynamics model calibrated using realistic CNT shapes encountered experimentally. The analysis shows that the shape and orientation of CNTs has a strong effect on the scattered electromagnetic response. We used the theory of characteristic modes (TCM) to explain this dependence of the scattered electromagnetic waves on the shape of the CNT. Using TCM, we developed simplified but highly accurate formulas that link the shapes of the CNTs to the resonances in their total extinction coefficient spectrum. These formulations have the potential to be the basis for advancing the nondestructive evaluation of CNT composites using electromagnetic waves as well as the development of novel CNT electromagnetic systems and devices.

**Index Terms**—Electromagnetic scattering, single-walled carbon nanotubes (CNTs), theory of characteristic modes (TCM).

## I. INTRODUCTION

CARBON nanotube (CNT) additives in composites exhibit a wide variety of complex shapes and are rarely perfectly straight even when they are highly aligned [1]. Moreover, fabrication capabilities have advanced enough to allow the synthesis of CNT additives with desired shapes such as helices, rings, and Y-shaped junctions [1]. The shape of CNTs has a profound effect on the mechanical properties of the composites as predicted by numerous simulations and measurements [2]. An example of such studies is the work by Fisher *et al.* who found

Manuscript received May 13, 2015; revised November 04, 2015; accepted January 10, 2016. Date of publication November 09, 2015; date of current version July 04, 2016. This work was supported in part by the National Institute of Standards and Technology project, “Carbon Nanocomposite Manufacturing: Processing, Properties, Performance,” and in part by the NIST Grant 70NANB15H285 “Multi-Scale Computational Modeling of Carbon Nanostructure Composites.”

A. M. Hassan is with the Computer Science and Electrical Engineering Department, University of Missouri-Kansas City, Kansas City, MO 64110 USA (e-mail: hassanam@umkc.edu).

F. Vargas-Lara and J. F. Douglas are with the Materials Science and Engineering Division, Material Measurement Laboratory, National Institute of Standards and Technology, Gaithersburg, MD 20899 USA (e-mail: luis.vargaslara@nist.gov; jack.douglas@nist.gov).

E. J. Garboczi is with the Applied Chemicals and Materials Division, Material Measurement Laboratory, National Institute of Standards and Technology, Boulder, CO 80305 USA (e-mail: edward.garboczi@nist.gov).

Color versions of one or more of the figures in this paper are available online at <http://ieeexplore.ieee.org>.

Digital Object Identifier 10.1109/TAP.2016.2526046

numerically that even the slightest curvature or “waviness” in the CNT can lead to a composite with mechanical properties that are significantly different from those of a composite with straight CNTs [2]. Regarding the electrical properties, Li *et al.* have shown that the scaling of the effective conductivity of the composite, with the volume fraction of the additive, is different for curved CNTs than for straight CNTs [3]. The thermal properties of CNT composites were also found to significantly depend on the *nonstraightness* of CNTs [4]. Finally, the effect of the CNT shape on the static electric and magnetic polarizability tensors has been recently quantified [5]. All this previous work has demonstrated the importance of accounting for CNT shape due to its influence on the mechanical, thermal, and electrical properties of composites. Similarly, it is necessary to quantify the effect of CNT shape on the composite’s electromagnetic scattering characteristics. This is important not only to understand how the electromagnetic response of the material depends on CNT structure but also because such an understanding may provide the basis for rapid measurements of composite structure, suitable for in-line manufacturing process control.

Quantifying the electromagnetic scattering characteristics of CNTs and CNT composites has received wide interest by several research groups [6]–[16]. The potential of straight CNTs as nanoantennas has been quantified by the seminal works of Hanson [7], Burke *et al.* [8], and Slepyan *et al.* [9]. Electromagnetic scattering characteristics of an infinite planar array of straight CNTs in the lower infrared band were reported in [10]. Sotiropoulos *et al.* studied the scattering characteristics of finite arrays of straight CNTs with different spatial distributions using the MOM solution of Hallén/Pocklington-type equations [11]. Experimental measurements and computational modeling of the interaction of electromagnetic waves with CNT composites were also reported in [12]–[15]. A two-dimensional (2-D) model, which studied how the randomness in the location of straight and parallel CNTs in a composite affects the electromagnetic response, was presented in [16].

But to the best of our knowledge, electromagnetic scattering from CNTs having realistic shapes has not been previously studied. More precisely, a direct relationship between CNT shape and its electromagnetic scattering characteristics has not been formulated. Therefore, the goal of this work is to understand the relationship between the shape of an individual three-dimensional (3-D) single-walled CNT (SWCNT) and the electromagnetic waves it scatters.

In this work, we employ the method-of-moments (MOM) formulation for arbitrary thin wires (ATW), as detailed in

[17], to quantify the electromagnetic scattering characteristics of individual SWCNTs with realistic shapes. In the MOM formulation for ATW, the 3-D CNT is approximated as a thin wire and current is assumed to flow only in the axial direction. We generated hundreds of worm-like cylinders, with realistic shapes for describing CNTs, using a coarse-grained molecular dynamics (MD) model. The parameters of the coarse-grained model were chosen to generate shapes of CNTs found in commercial composite materials.

The MOM analysis of the worm-like CNTs shows that the CNT shape has a strong effect on the resonances in the total extinction-coefficient spectrum. These resonances are explained using the theory of characteristic modes (TCM) [18]–[23]. The TCM was first developed by Garbacz [18] and advanced by Harrington *et al.* for both perfect electric conducting (PEC) particles [19], [20] and for general dielectric and magnetic particles [21]. The TCM is based on decomposing the current flowing through an antenna or a scatterer into a set of orthogonal characteristic currents or modes, which are typically calculated through the solution of an eigenvalue problem [18]–[23]. The TCM has been employed to calculate the characteristic currents and explain the scattering properties of various PEC structures such as narrow and wide metal plates [22]. Recently, TCM has received a surge in interest in designing antennas with optimized properties [23]–[25]. In the TCM, the eigenvalue problem is solved at each frequency, yielding frequency-dependent eigenvalues and eigencurrents. Raines *et al.* have developed a method to track the characteristic modes over a wide frequency range [26]. Wu *et al.* have studied the evolution of the eigenvalues and the eigencurrents for small scatterers [27]. They have showed that, for small scatterers, the eigencurrents stay approximately unchanged, whereas the eigenvalues change with a cubic relationship with respect to frequency [27]. One of the main contributions of this work is the use of the TCM in simplifying the relationship between the shape of a CNT and the characteristics of the electromagnetic waves it scatters.

## II. MATHEMATICAL MODEL

### A. Coarse-Grained MD Model

Until recently, it has been extremely difficult to reconstruct the (3-D) shape of CNTs in an actual composite material [28]. Therefore, each CNT configuration considered in this work was generated by using MD simulations of a bead-spring model [29], [30]. In this model, each CNT is represented by  $N$ -connected spherical particles “beads” as shown in Fig. 1(a). A swept tube was then generated to enclose the beads, as shown in Fig. 1(a) and (b), which generates a worm-like cylindrical CNT similar to those previously reported [31]–[34]. Every bead represents several carbon atoms and, therefore, the model is coarse-grained since it does not simulate every carbon atom in the CNT. In the MD simulations performed, the excluded volume (EV) interaction among all the beads is given by a truncated and shifted 12-6 Lennard-Jones potential ( $U_{EV}$ ) [29], [30]

$$U_{EV}(r) = \begin{cases} 4\epsilon \left[ \left(\frac{\sigma}{r}\right)^{12} - \left(\frac{\sigma}{r}\right)^6 \right] + \epsilon, & \text{for } r < 2^{1/6}\sigma \\ 0, & \text{for } r > 2^{1/6}\sigma \end{cases} \quad (1)$$

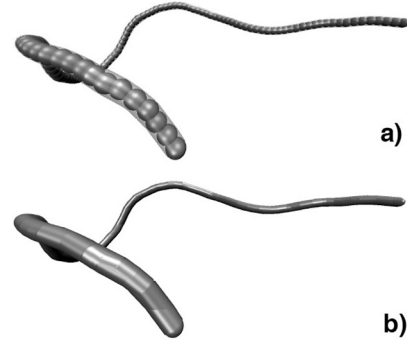


Fig. 1. Bead-spring model and swept tube model for the CNT. In (a), the walls of the swept tube are made transparent to show the beads they enclose, whereas in (b), the walls of the swept tube are made opaque to show the actual worm-like CNT simulated.

where  $r$  is the distance between any two beads,  $\sigma$  and  $\epsilon$  are the Lennard-Jones characteristic parameters representing the length and energy, respectively [29], [30]. The beads that form the CNT are connected by a finitely extensible nonlinear elastic ( $U_{FENE}$ ) potential

$$U_{FENE}(r) = -\frac{1}{2}k_{FENE} \left(\frac{3}{2}\sigma\right)^2 \log \left\{ 1 - \left[\frac{r}{1.5\sigma}\right]^2 \right\}. \quad (2)$$

Here, we chose  $k_{FENE} = 30\epsilon/\sigma^2$ , as the strength of the bonding energy. Additionally, neighboring connected beads along the CNT interact via an angular potential

$$U_{ang}(\theta) = k_{ang}(1 - \cos\theta) \quad (3)$$

where  $k_{ang}$  is the bending constant, and  $\theta$  is the angle formed by three consecutive beads that form the CNT. Equations (1)–(3) generate CNTs whose shapes are worm-like chains similar to the one shown in Fig. 1. The applicability of the bead-spring model in describing CNTs geometries is based on the fact that CNTs may be aptly described as one-dimensional (1-D) polymers. This was demonstrated by Vargas-Lara and Douglas [35], and Lee *et al.* [31] and [32] where the bead spring model provided an experimentally validated model of the true geometrical structure of both isolated single and multiwall CNTs. Using the interaction potentials described in (1)–(3), we integrate Newton’s equations of motion, for each bead in the CNTs, at a fixed temperature for periods of time  $\geq 10^6$  time steps, after which the CNTs reach their thermal equilibrium [29], [30]. We compute the electromagnetic resonance only for CNT shapes that have reached thermal equilibrium because, by that time, the shape properties of the CNTs reach the desired values regulated by the parameters in (1)–(3). Further details on the implementation of the bead-spring model can be found in [29] and [30].

By varying the parameter  $k_{ang}$ , CNTs with different persistence lengths ( $P$ ) can be generated. The value of  $P$  is a measure of the stiffness of the CNT [36]. That is, the higher the value of  $P$ , the more difficult it is to bend the CNT and therefore, the CNTs will be straighter. On the other hand, low values of  $P$  indicate that the CNTs are more flexible and therefore the CNTs will exhibit high curvatures and bends. Therefore, the persistence length is a measure of the waviness of the CNT. Four different  $k_{ang}$  values were considered in this work: 9, 40, 80,

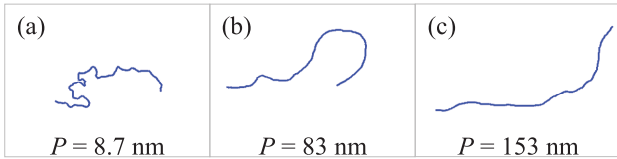


Fig. 2. Worm-like CNTs with equal length  $L = 193$  nm and persistence lengths (a)  $P = 8.7$  nm, (b)  $P = 83$  nm, and (c)  $P = 153$  nm.

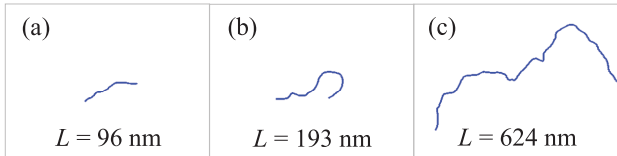


Fig. 3. Worm-like CNTs with persistence length  $P = 83$  nm and lengths (a)  $L = 96$  nm, (b)  $L = 193$  nm, and (c)  $L = 624$  nm.

and 120. These correspond to the following values of  $P$ : 8.7, 35, 83, and 153 nm. These values are comparable to those reported in [31] and [32]. Fig. 2 shows three CNTs with equal contour lengths  $L = 193$  nm but with different values of  $P$ . Fig. 2(a) shows the CNT with the lowest value of  $P$  and, therefore, it is highly contorted, whereas the CNT in Fig. 2(c), with the highest persistence length, is the straightest. The CNT shapes shown in Figs. 1 and 2 are similar to the shapes exhibited in commercial CNT samples [33] and in certified CNT reference materials [34].

In all the cases studied in this work, the parameter  $\sigma$  was set to be  $\sigma \approx 0.96$  nm, which yields CNTs with lengths  $L \approx 0.96N$  nm. The radius of the beads was estimated to be 0.61 nm to resemble the radius  $\rho$  of the metallic (9, 9) armchair SWCNT. Five different CNT contour lengths were generated in this work by varying the number of beads  $N$ :  $L = 96$  nm,  $L = 193$  nm,  $L = 384$  nm,  $L = 624$  nm, and  $L = 831$  nm. These values of contour lengths were selected to be comparable to the CNT contour lengths exhibited in commercial samples [33] and in certified CNT reference materials [34]. Three CNTs with contour lengths  $L = 96$  nm,  $L = 193$  nm, and  $L = 624$  nm are shown in Fig. 3. All three CNTs in Fig. 3 have the same value of  $P = 83$  nm. For each CNT length  $L$  and value of  $P$ , 100 different shapes were generated using the coarse-grained MD model. This large number of shapes is considered to realistically encompass the possible variations in CNT shape for each length and persistence length. Moreover, the 100 shapes in each set were selected from a much larger pool of 1000 shapes such that the selected 100 shapes have the same statistical distribution of end-to-end distances as the original 1000 shapes. All the CNTs had exactly the same radius ( $\rho = 0.61$  nm) and the same conductivity of the metallic (9, 9) armchair CNT, as will be described in the following section.

## B. MOM for ATW

In this work, we employ the standard MOM in the ATW formulation to simulate the electromagnetic scattering from our model CNTs [17]. All the CNTs considered are embedded in

free space and are excited by an incident plane wave propagating with wavelength  $\lambda_0$  and with an incident electric field  $\mathbf{E}^i$ . In the ATW formulation, the 3-D CNT, with radius  $\rho$  and length  $L$  is modeled as a wire based on the assumption that current excited by the incident  $\mathbf{E}^i$  will flow only in the axial direction [17]. This assumption is valid when the length of the scatterer and the wavelength of the incident wave are much larger than the radius,  $L > 20\rho$  and  $\lambda_0 > 20\pi\rho$  [37], which is valid in CNT applications and for electromagnetic waves with wavelengths longer than the vacuum ultraviolet region [10], [11]. Our implementation of the MOM for ATW was validated exhaustively by comparing with published results [17] and by comparing with the results achieved using commercial electromagnetics packages.

The axial conductivity of CNTs  $\sigma_{\text{cnt}}$  is finite and can be expressed in the Drude model as [38], [39]

$$\sigma_{\text{cnt}} \cong \frac{\sigma_0}{1 + j\omega\tau}, \quad \sigma_0 = \frac{2e^2 v_F \tau}{\pi^2 \hbar \rho} \quad (4)$$

where  $e$  is the electron charge,  $v_F$  is the Fermi velocity,  $\hbar$  is the normalized Planck's constant,  $\tau$  is the relaxation time, and  $j$  is  $\sqrt{-1}$ . The axial surface conductivity in (4) is only valid in the microwave and terahertz range for metallic CNTs with small chirality indices  $(n, m) < 50$  [38], [39]. In this work, the (9, 9) armchair CNT with radius  $\rho = 0.61$  nm is employed in all the cases considered. The values  $v_F = 9.71 \times 10^5$  m/s and  $\tau = 3$  ps, employed in (4), are similar to values in [7]. The distributed impedance of the CNT,  $Z_{\text{CNT}}$ , can be then expressed as [39]

$$Z_{\text{CNT}} = \frac{1}{2\pi\rho\sigma_{\text{CNT}}} = R_{\text{CNT}} + j\omega L_{\text{CNT}} \quad (5a)$$

$$R_{\text{CNT}} = \frac{1}{2\pi\rho\sigma_0}, \quad L_{\text{CNT}} = \frac{\tau}{2\pi\rho\sigma_0} \quad (5b)$$

where  $R_{\text{CNT}}$  is the Ohmic distributed resistance and  $L_{\text{CNT}}$  is the kinetic inductance of the CNT [39].

The accuracy of the above model for the CNT conductivity  $\sigma_{\text{cnt}}$  has been validated using several experiments [10], [12]–[15]. There is evidence that the conductivity of a curved CNT should be similar to that of a straight CNT as long as the bends in the CNTs are not too sharp as comprehensively studied in [40]. In [40], two different kinds of bending or curves in CNTs were defined. In the first kind, termed localized deformation, the bending was created by exerting a local force, e.g., through an AFM tip. In the second kind, termed delocalized deformation, the bending force was distributed over a wider length of the tube similar to the force distribution created when a CNT is deformed by bending its two ends. The first kind of deformation can lead to kinks in the CNT wall with a significant effect on the conductivity even for nonsharp bends. In the second kind of deformation, which is the kind relevant to this work, the distribution of the bending force over a larger spatial extent leads to a small effect on the conductivity as long as the radius of curvature of the deformation is larger than a certain critical radius. If the radius of curvature is smaller than the critical radius, created by bending the CNT into a tighter circle, kinks start to appear in the walls of the CNT similar to those created by localized

deformation. The critical radius of curvature for a (5, 5) armchair CNT was on the order of 1.76 nm [40]. The mean radius of curvature of the CNTs considered in this work is equivalent to the persistence length. The minimum persistence length considered in this work is 8.7 nm, which is larger than the critical radius of 1.76 nm. Therefore, we anticipate no dramatic change in conductivity at the levels of persistence lengths considered. If variations in conductivity were to be incorporated, we anticipate that the effect of the shape on the electromagnetic response of CNTs will be further magnified. Therefore, the conductivity given by (4) will be used in all the shapes simulated.

Since the CNTs have irregular shapes and random orientations, the scattered electromagnetic waves are not uniform in all directions for a given incident direction. Therefore, it is important to consider all scattering directions through the use of the extinction power  $P_{ext}$ . The extinction power is calculated as the sum of: 1) the power absorbed and 2) the power scattered by the CNT in all directions. The extinction power  $P_{ext}$  can be expressed as [41]

$$P_{ext} = 0.5\text{Re} \left( \int \mathbf{I}^* \cdot \mathbf{E}^i d\ell \right) \quad (6)$$

where the  $*$  notation refers to the conjugate transpose. The extinction power is typically normalized by the power density of the incident plane wave to yield the total extinction cross section  $C_{ext}$ . The power density of the incident plane wave can be expressed as  $|\mathbf{E}^i|^2 / 2\eta$  and, therefore,  $C_{ext}$  can be expressed as follows:

$$C_{ext} = \frac{P_{ext}}{|\mathbf{E}^i|^2 / 2\eta} = \frac{0.5\text{Re} \left( \int \mathbf{I}^* \cdot \mathbf{E}^i d\ell \right)}{|\mathbf{E}^i|^2 / 2\eta} \quad (7)$$

where  $\eta = \sqrt{\mu/\epsilon}$  is the impedance of the medium where the CNTs are embedded.

### III. NUMERICAL RESULTS

#### A. Electromagnetic Scattering From CNTs With Simple Shapes

In this section, the total extinction coefficient is calculated versus frequency for CNTs with simple shapes. In particular, we will focus on the resonances in the total extinction coefficient  $C_{ext}$ , as the  $C_{ext}$  at the resonance is greater by a factor of 100 or more than the  $C_{ext}$  at the frequencies between resonances. We investigate CNTs with the following three shapes: 1) straight; 2) C-shaped; and 3) helical as shown in Fig. 4. The simplicity of these shapes will provide a starting point to show how the shape of the CNTs affects the resonances in the scattered electromagnetic waves. Moreover, C-shaped and helical CNTs have been fabricated before, so these shapes have importance of their own [1]. In the three cases shown in Fig. 4, the incident wave had exactly the same direction and polarization. Also, the three CNT shapes have exactly the same radius  $\rho = 0.61$  nm, length  $L = 193$  nm, and conductivity  $\sigma_{CNT}$  as given by (4). Fig. 4 shows the extinction coefficient from these cases as a function of frequency. Fig. 4 clearly indicates that the shape of the CNT has a strong effect on its electromagnetic scattering characteristics.

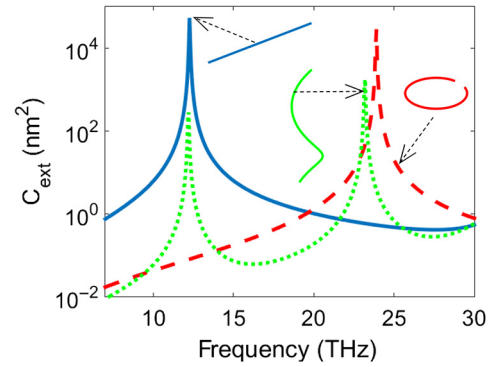


Fig. 4. Extinction coefficient of (a) straight, (b) C-shaped, and (c) helix-shaped CNT. The three CNT shapes had the same excitation and length.

Typical straight wire scatterers resonate at frequencies that occur at the following wavelengths:

$$\lambda_0 = \frac{2L}{\alpha m}, \quad m = 1, 2, 3, \dots \quad (8)$$

where  $\lambda_0$  is the wavelength in free space and  $\alpha$  is the velocity factor. The value of  $\alpha$  is very close to unity for the PEC case [42]. For CNTs with finite length, plasmon frequencies in the THz range were experimentally demonstrated for the first time in [12]–[15]. The plasmon frequencies typically occur at wavelength significantly larger than the CNT length [12]–[15]. Therefore, the velocity factor  $\alpha$  in (8) typically varies in the range of 0.01–0.02 for CNTs [7]. To determine the velocity factor, consider the straight CNT whose first resonance in the total extinction coefficient occurs around 12.3 THz, which corresponds to a velocity factor  $\alpha = 0.016$ . Using this value for the velocity factor in addition to (8), the first three resonances should occur approximately around the following wavelengths:  $\lambda_1 = 24 \mu\text{m}$ ,  $\lambda_2 = 12 \mu\text{m}$ , and  $\lambda_3 = 8 \mu\text{m}$ . These wavelengths correspond to *approximately* the following frequencies at the first three resonances:  $f_1 = 12.3$  THz,  $f_2 = 24.9$  THz,  $f_3 = 37.3$  THz.

For the straight CNT, the extinction coefficient has a first resonance around 12.3 THz but no second resonance as shown in Fig. 4. This will be justified by the TCM analysis in the following section. The first resonance is absent in the C-shaped CNT and it only has a second resonance around 23.7 THz as shown in Fig. 4. The helical CNT has two resonances at different peak amplitude than either the straight or the C-shaped CNTs but centered at approximately the same positions:  $f_1 = 12.2$  THz and  $f_2 = 23.2$  THz. These three cases show that the CNT shape has a strong effect on electromagnetic scattering. Furthermore, Fig. 4 suggests that the peak amplitudes of the resonances might contain information about the shape of the CNTs. These results are corroborated in the following section by simulating worm-like CNTs with realistic morphologies.

#### B. Electromagnetic Scattering From CNTs With Realistic Shapes

Realistic worm-like CNTs were simulated using the coarse-grained MD model described in Section II. We will first start with the case where the CNT length  $L = 193$  nm, the persistence length  $P = 83$  nm, and the conductivity  $\sigma_{CNT}$  is

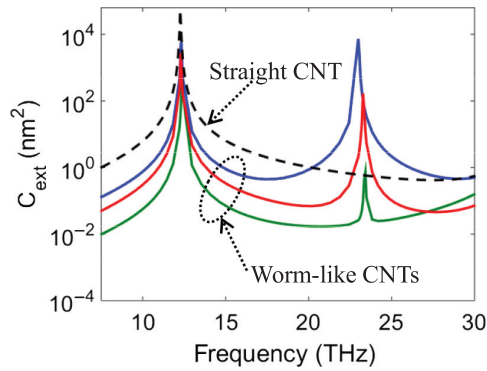


Fig. 5. Total extinction coefficient versus frequency for three CNTs of different shapes each shown as a solid thin line using different colors to separate the different curves. The extinction coefficient of a straight CNT of the same length and radius and for the first resonance is also shown as a thick dashed black line.

given by (4). The incident wave is propagating in the negative  $z$ -direction, polarized in the  $x$ -direction and the CNTs are embedded in free space. A total of 100 different shapes were considered. The CNTs are randomly oriented with no sense of alignment.

Fig. 5 shows the extinction coefficient for 3 of the 100 CNT shapes considered in the frequency range from 7 to 30 THz, covering the first two resonances. Each of these three cases is shown as a solid line, with three different line colors used to help indicate different CNT shapes. The extinction coefficient of a straight CNT, for the first resonance since the straight CNT does not have a second resonance, is shown as a thick dashed line for comparison. From Fig. 5 and from the study of all the different 100 CNT shapes, it is clear that all the CNTs resonate at the same frequency for the first two resonances even though they consisted of a wide variety of shapes. Therefore, the shape of the CNT has a minimal effect on the resonance frequency and the resonance frequency seems to be only dependent on the total length and the conductivity of the scatterer [43]. Fig. 5, however, shows a wide variation in the peak amplitude of the resonances from the CNTs. Therefore, the CNT shape must have a strong effect on the peak amplitude of the first and second resonance.

To quantify the effect of the persistence length on the electromagnetic scattering characteristics, we will use the same length  $L = 193$  nm and consider the following values for the persistence length:  $P = 8.7$  nm,  $P = 35$  nm,  $P = 83$  nm, and  $P = 153$  nm. One hundred different shapes for each persistence length value are considered. The pristine CNT shapes generated using the model in Section II are randomly oriented. However, for the comparison between the different persistence values to be useful, the CNTs need to be aligned in one direction. The alignment of the CNTs is necessary because two CNTs with exactly the same shape can yield completely different total extinction coefficient values depending on their orientation with respect to the incident wave. For example, if the incident wave is propagating in the negative  $z$ -direction and polarized in the  $x$ -direction, a straight CNT oriented parallel to the  $y$ -axis will scatter zero power at the first resonance frequency. A straight CNT oriented parallel to the  $x$ -axis will scatter a maximum value for the total extinction coefficient at

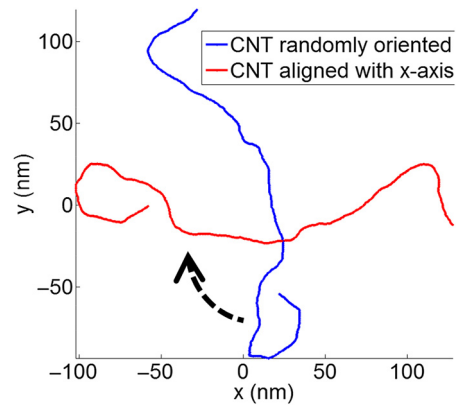


Fig. 6. Rotation of a CNT of length  $L = 384$  nm and persistence length  $P = 83$  nm to align it with the  $x$ -axis.

the first resonance frequency. Therefore, to study only the effect of the shape, the CNTs need to be aligned. However, it is hard to define alignment for complex shapes like the shapes of the CNTs considered in this work as shown in Figs. 1–3. One way to impose an approximate alignment is to calculate the gyration tensor  $\mathbf{S}$  for each CNT as defined in [44]. If the CNT has a general orientation, then the nine components of the gyration tensor can be nonzero. To achieve alignment, the CNT is rotated until the gyration tensor is diagonal and  $S_{xx} \geq S_{yy} \geq S_{zz}$ . In this orientation, if the CNT is fit within a tri-axial ellipsoid, the major axis of this ellipsoid will be aligned in the  $x$ -direction, which is the same direction as the incident electric field. An illustration of this process is shown in Fig. 6.

After all the CNT shapes were aligned with the  $x$ -axis in this manner, the total extinction coefficient was calculated. Fig. 7 shows a histogram of the peak amplitude of the first resonance for the four different persistence length values considered. One hundred different shapes were considered for each of the four persistence length values, and for all the shapes, the incident wave is propagating in the negative  $z$ -direction and the electric field is polarized parallel to the  $x$ -axis. Considerable spread in the peak amplitude values can be seen in all four persistence values considered as shown in Fig. 7(a)–(d). Therefore, it is important to take into consideration the shape of the CNTs when designing or testing CNT devices and composites. As the persistence length increases, the peak amplitude of the first resonance increases as indicated by the progression from Fig. 7(a)–(d).

Fig. 8 shows the average of the peak amplitudes of the first and second resonances versus the persistence length. Two different polarizations are considered:  $\mathbf{E}^i$  parallel to the  $x$ -axis and  $\mathbf{E}^i$  parallel to the  $y$ -axis. Each data point in Fig. 8 corresponds to the average peak amplitude of 100 different CNT shapes. The average peak amplitude of the first resonance, when  $\mathbf{E}^i$  is parallel to the  $x$ -axis, is much larger than the average peak amplitude of the first resonance when  $\mathbf{E}^i$  is parallel to the  $y$ -axis. This is anticipated since the CNTs are aligned parallel to the  $x$ -axis. Also, when  $\mathbf{E}^i$  is parallel to the  $x$ -axis, the average peak amplitude of the first resonance increases as the persistence length increases. Therefore, the straighter the CNT, the larger the total

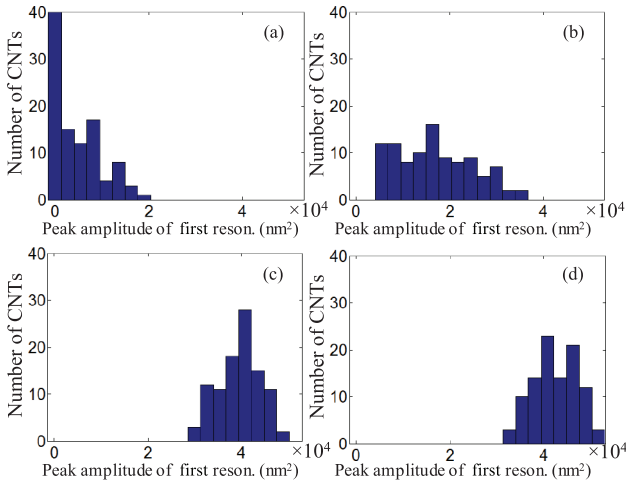


Fig. 7. Histogram of the peak amplitude of the first resonance for a CNT with length  $L = 193$  nm and persistence lengths: (a)  $P = 8.7$  nm; (b)  $P = 35$  nm; (c)  $P = 83$  nm; and (d)  $P = 153$  nm.

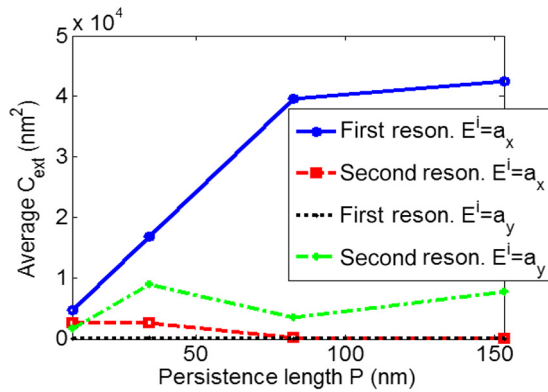


Fig. 8. Average peak amplitude of the first and second resonance for two different polarizations. All CNTs have the same contour length  $L = 193$  nm. Each data point corresponds to the average of 100 different shapes.

extinction coefficient at the first resonance frequency. The average peak amplitude of the first resonance saturates beyond the persistence length  $P = 83$  nm. This can be explained by the fact that, for  $P > 83$  nm, the CNTs are close to a perfectly straight CNT and the average peak amplitude of the first resonance will converge to that of a straight CNT. The average peak amplitude of the second resonance, when  $\mathbf{E}^i$  is parallel to the  $x$ -axis, decreases as the persistence length increases or as the CNTs become straighter, whereas there is no regular trend in the peak amplitude of the second resonance, when  $\mathbf{E}^i$  is parallel to the  $y$ -axis.

To quantify the effect of the actual CNT length  $L$  on the electromagnetic scattering characteristics, Fig. 9 shows a histogram of the peak amplitude of the first resonance for:  $L = 96$  nm,  $L = 193$  nm,  $L = 384$  nm,  $L = 624$  nm, and  $L = 831$  nm. One hundred different shapes were considered for each of the five contour length values and all the shapes were oriented parallel to the  $x$ -axis as shown in Fig. 6. All the CNTs in Fig. 9 had the same persistence length  $P = 83$  nm. Considerable spread in the peak amplitude values can be seen

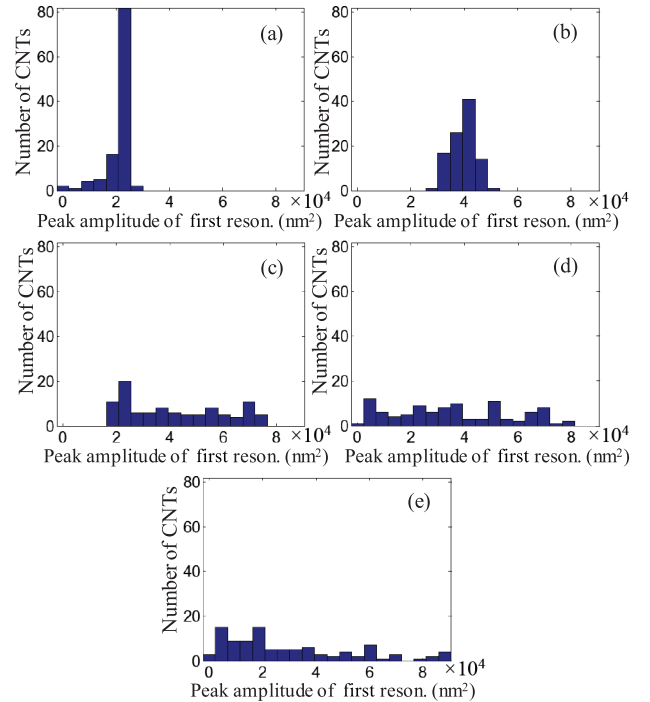


Fig. 9. Histogram of the peak amplitude of the first resonance for CNTs with persistence length  $P = 83$  nm and contour lengths: (a)  $L = 96$  nm; (b)  $L = 193$  nm; (c)  $L = 384$  nm; (d)  $L = 624$  nm; and (e)  $L = 831$  nm.

in all four persistence values considered as shown in Fig. 9(a)–(e). The spread in the peak amplitude increases as the contour length of the CNT increases. For example, Fig. 9(a), which corresponds to the shortest CNT  $L = 96$  nm, shows that the peak amplitudes are spread between 372 and 25704 nm<sup>2</sup>. Fig. 9(e), which corresponds to the longest CNT,  $L = 831$  nm, shows that the peak amplitudes are spread over a wider range between 238 and 88248 nm<sup>2</sup>. This can be explained by the fact that as the CNTs get longer, they can exhibit a wider variability in their shape, which corresponds to a larger range of possible values for the peak amplitudes of the first resonance of the total extinction coefficient.

Fig. 10 shows the average of the peak amplitudes of the first and second resonances, versus the CNT contour length, using the same data in Fig. 9. Two different polarizations are considered:  $\mathbf{E}^i$  parallel to the  $x$ -axis and  $\mathbf{E}^i$  parallel to the  $y$ -axis. All the CNTs in Fig. 10 are aligned parallel to the  $x$ -axis and each data point in Fig. 10 corresponds to the average of 100 different shapes. Similar to Fig. 8, Fig. 10 shows that the average peak amplitude of the first resonance when  $\mathbf{E}^i$  is parallel to the  $x$ -axis is much larger than the average peak amplitude of the first resonance when  $\mathbf{E}^i$  is parallel to the  $y$ -axis for all values of  $L$ . Also, when  $\mathbf{E}^i$  is parallel to the  $x$ -axis, the average peak amplitude of the first resonance increases until  $L = 384$  nm and then it starts declining. The average peak amplitude of the second resonance, when  $\mathbf{E}^i$  is parallel to the  $x$ -axis, increases as the length of the CNT increases. On the other hand, the average peak amplitude of the second resonance, when  $\mathbf{E}^i$  is parallel to the  $y$ -axis, increases as the length of the CNT increases up to  $L = 384$  nm and then it starts decaying.

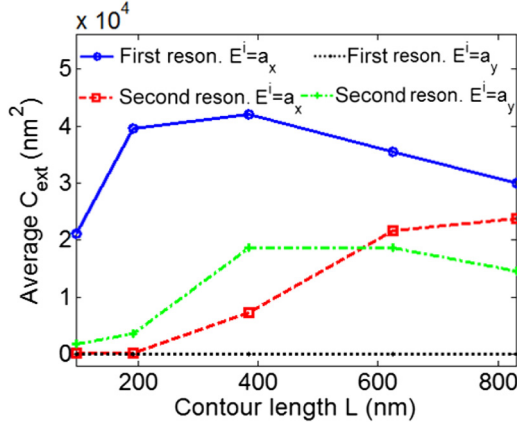


Fig. 10. Average peak amplitude of the first and second resonance for two different polarizations. All CNTs have the same persistence length  $P = 83$  nm. Each data point corresponds to the average of 100 different shapes.

In the following section, we will use the TCM to explain the trends in Figs. 4–10. We will also link the CNT shape with peak amplitudes of the resonance allowing us to predict, without full-wave analysis, which shapes will generate a large or small first/second resonance.

#### IV. TCM FOR CNTS ELECTROMAGNETIC SCATTERING

The TCM is based on the eigenvalue problem [20]

$$\mathbf{X}\mathbf{J}_n = \lambda_n \mathbf{R}\mathbf{J}_n \quad (9)$$

where  $\mathbf{X}$  and  $\mathbf{R}$  are the imaginary and real parts, respectively, of the MOM impedance matrix as defined in [17]. The vectors  $\mathbf{J}_n$  are the eigencurrents, also termed modes or characteristic currents, and  $\lambda_n$  are the eigenvalues. Both the eigenvalues  $\lambda_n$  and the eigencurrents  $\mathbf{J}_n$  are real and frequency dependent, since the matrices  $\mathbf{X}$  and  $\mathbf{R}$  vary with frequency. The eigenvalue problem (9) is solved, for each frequency, using the procedure detailed by Harrington and Mautz [20]. The current flowing in the CNT  $\mathbf{I}$  can be expressed as a function of the eigenvalues and the eigencurrents as follows:

$$\mathbf{I} = \sum_n \frac{V_n \mathbf{J}_n}{(1 + j\lambda_n) \langle \mathbf{J}_n, \mathbf{R}\mathbf{J}_n \rangle} \quad (\text{A}) \quad (10a)$$

$$V_n = \int \mathbf{J}_n \cdot \mathbf{E}^i dl \quad (\text{W}) \quad (10b)$$

$$\langle \mathbf{J}_n, \mathbf{R}\mathbf{J}_n \rangle = \int \mathbf{J}_n \cdot (\mathbf{R}\mathbf{J}_n) dl \quad (\text{W}) \quad (10c)$$

where  $V_n$  is called the modal excitation coefficient (MEC) and  $\langle \mathbf{J}_n, \mathbf{R}\mathbf{J}_n \rangle$  is a normalization factor. The MEC  $V_n$  describes the capability of the incident electric field  $\mathbf{E}^i$  to excite the eigencurrent  $\mathbf{J}_n$ . That is, if the incident electric field is oriented with respect to the shape of the CNT, such that the eigencurrent  $\mathbf{J}_n$  cannot be generated, then  $V_n = 0$ . If, however, the current  $\mathbf{J}_n$  is strongly excited by the incident electric field, then  $V_n$  will have a large value. An important advantage of the representation in (10) is that the entire dependence on the orientation of the CNT or the direction of the incident electric field is encapsulated in  $V_n$ . The eigenvalues  $\lambda_n$  and the normalization factor

$\langle \mathbf{J}_n, \mathbf{R}\mathbf{J}_n \rangle$  are completely independent of the orientation of the CNT or the direction of the incident electric field.

At any given frequency, not all eigencurrents will contribute equally to the current  $\mathbf{I}$  in (10a). The significance of each eigencurrent, termed the modal significance ( $MS_n$ ) factor, can be defined as

$$MS_n = \frac{1}{|1 + j\lambda_n|}. \quad (11)$$

The normalization factor  $\langle \mathbf{J}_n, \mathbf{R}\mathbf{J}_n \rangle$  is added such that each mode will generate unity power if excited.

Using the TCM representation, the extinction coefficient  $C_{ext}$  can be expressed in terms of the eigencurrents, the eigenvalues, and the MEC as follows:

$$C_{ext} = \frac{\eta}{|\mathbf{E}^i|^2} \sum_n \left( \frac{MS_n^2 |V_n|^2}{\langle \mathbf{J}_n, \mathbf{R}\mathbf{J}_n \rangle} \right) \quad (12)$$

where  $\eta$  is the impedance of the medium where the CNT is embedded taken to be free space in this work. The various terms in the TCM, shown in (9)–(12), have been explored extensively for a variety of antennas [23]–[25]. However, the contribution of this work is that they are calculated, for the first time, for CNTs with realistic shapes and finite conductivity. All the CNTs considered in this work are assigned a finite axial conductivity  $\sigma_{\text{CNT}}$  as expressed by the Drude model in (4).

In the following sections, we will summarize the results from the TCM analysis of CNTs. In particular, we will explore how the main factors of the TCM decomposition,  $V_n$ ,  $MS_n$ , and  $\langle \mathbf{J}_n, \mathbf{R}\mathbf{J}_n \rangle$  vary with the shape and orientation of the CNTs.

##### A. Modal Significance $MS_n$

Fig. 11(a) shows the  $MS_n$  for the first three modes for a straight perfectly conducting (PEC) wire of length  $L = 193$  nm and radius  $\rho = 0.61$  nm. Fig. 11(b) shows the  $MS_n$  for a straight CNT with the conductivity expressed by the Drude model in (4). The dimensions of the PEC wire in Fig. 11(a) and the CNT in Fig. 11(b) are identical. Also, it is important to emphasize that the  $MS_n$  is independent of the CNT orientation or the direction and polarization of the incident plane wave. From Fig. 11(a), the first three resonance frequencies for the PEC wire are 730, 1490, and 2260 THz. At the first resonance,  $MS_1$  is close to unity, whereas  $MS_2$  and  $MS_3$  are much smaller. This means that at the first resonance, the current is very close to the current of the first eigencurrent. In the second resonance,  $MS_2$  is close to unity, whereas  $MS_1$  is approximately 0.3627 and  $MS_3$  is negligible. This means that at the second resonance, the current can be a mixture of the second eigencurrent and the first eigencurrent, depending on the MEC of each eigencurrent, with the second eigencurrent having more weight than the first eigencurrent. Finally, the third resonance can be a mixture of the three eigencurrents with the third eigencurrent having a weight of 1 and the first and second eigencurrents have an equal weight of 0.39.

By comparing Fig. 11(b) with Fig. 11(a), it is clear that the response of the still straight CNT is significantly different from that of a PEC wire with the same dimensions. The first three

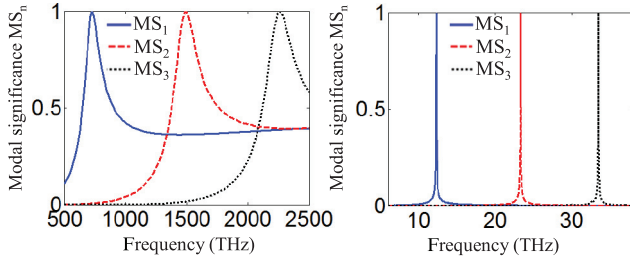


Fig. 11. Modal significance factors of a straight (a) PEC wire and (b) CNT with the same dimensions.

resonances occur at the much lower frequencies of 12, 23, and 33 THz and are much narrower. The ratio between the resonance frequency of a CNT and the resonance frequency of a PEC with the same shape and dimensions is termed the velocity factor  $\alpha$ . In Fig. 11(b),  $\alpha \approx 0.016$  which is in agreement with the range  $\alpha \approx 0.01$  to  $0.02$ , observed in several previous studies [7]. Therefore, CNTs resonate at a very low frequency in comparison to their length. This fact will be used to simplify the shape dependence of the total extinction coefficient at the resonances in the following sections. This shift to lower frequencies is due to the significant inductance term in the impedance of the CNTs as shown in (5). This inductance slows the wave propagating along the CNT shifting the resonances to lower frequencies [7]. Also, the CNT resonances are significantly narrower than those of the PEC wire. The widths of the resonances are controlled by the Ohmic distributed resistance or the real part of the distributed impedance of the CNTs,  $R_{CNT}$ , as expressed in (5b). The peaks become broader as the value of  $R_{CNT}$  increases. The main goal of this work is to quantify the effect of shape on the electromagnetic response of CNTs. Therefore, we will defer investigating the effect of variations in the conductivity  $\sigma_{CNT}$ , which will lead to variations in  $R_{CNT}$  and  $L_{CNT}$ , to future work.

Similar to the PEC wire, at the first resonance, the current  $MS_1$  is close to unity, whereas  $MS_2$  and  $MS_3$  are much smaller. This means that at the first resonance, the current of the CNT is very close to the current of the first eigencurrent  $J_1$ . However, the second and third resonances for the CNT differ significantly from the PEC wires. For the CNT, at the second resonance,  $MS_2$  is close to unity, whereas  $MS_1$  and  $MS_3$  are negligible. Therefore, the current at the second resonance is very close to the second eigencurrent. This is in contrast to the PEC wire where the current at the second resonance can be a mixture of the second and first eigencurrent. Also, at the third resonance,  $MS_3$  is close to unity, whereas  $MS_1$  and  $MS_2$  are negligible. Therefore, for CNTs, the current at the third resonance is mainly due to the third eigencurrent, whereas for the PEC wire, the current at the third resonance is a mixture of the first three eigencurrents. Therefore, the main contribution from the TCM analysis in this section is that, for CNTs, the current at each resonance is *purely* described by a single eigencurrent. The fact that the current is not a function of a mixture of eigencurrents, at a resonance, significantly simplifies the dependence of the peak amplitude on the shape of the CNT as will be detailed in the following section. Even though Fig. 11 was for a straight

CNT, our analysis of hundreds of different shapes has shown a similar behavior.

The eigencurrents:  $J_1$  at the first resonance and  $J_2$  at the second resonance are shown in Fig. 12(a) and (b), respectively, for 100 different worm-like CNT shapes of contour length  $L = 193$  nm and persistence length  $P = 83$  nm. The same eigencurrents are shown for 100 different worm-like CNT shapes all having  $L = 624$  nm and  $P = 83$  nm in Fig. 12(c) and (d). Also, to facilitate the comparison between the different shapes, the eigencurrents are normalized such that they have a maximum amplitude of unity and they are plotted versus the normalized CNT length  $\ell$  which varies from 0 at the beginning of the wire to 1 at its end. Fig. 12 shows that the normalized eigencurrents can be approximated as

$$J_n \approx \sin(n\pi\ell) \quad (13)$$

where  $0 < \ell < 1$ . The approximation in (13) is shown as a thick dashed black line in each of the four parts of Fig. 12. Similar approximations for the eigencurrents have been previously presented for *uniform* structures as shown, e.g., in [22]. By inspecting Fig. 12(a) and (b), it is clear that the approximation in (13) is valid for all 100 CNT shapes with contour length  $L = 193$  nm. Fig. 12(c) and (d) shows that a few shapes yield characteristic currents that are considerably different from the approximation in (13). However, the approximation in (13) is still accurate for most of the CNT shapes of length  $L = 624$  nm. Therefore, the contribution in Fig. 12 is to show that the eigencurrents for CNTs with realistic conductivity and with *complex shapes* yield sinusoidal eigencurrents as approximated by (13) except for a few shapes with length  $L \geq 624$  nm. The accuracy of (13) will be further demonstrated in the following sections.

It is important to emphasize that the eigencurrents in Fig. 12 are *amplitude normalized* such that their maximum amplitude is unity to facilitate the comparison between different shapes. However, for (10) to be valid, the characteristic currents need to be normalized with another factor  $\langle \mathbf{J}_n, \mathbf{R}\mathbf{J}_n \rangle$ , which will be the focus of the following section.

### B. Normalization Factor $\langle \mathbf{J}_n, \mathbf{R}\mathbf{J}_n \rangle$

To evaluate the normalization factor  $\langle \mathbf{J}_n, \mathbf{R}\mathbf{J}_n \rangle$  for CNTs, we need to examine the real part of the impedance matrix  $\mathbf{R}$  calculated using the MOM formulation. As described in [17], the MOM impedance matrix is generated by dividing the CNTs into  $N$  segments each of length  $\Delta$ . For wires that are not perfectly conducting, the diagonal elements of the impedance matrix should be augmented with a term proportional to the CNT impedance [17]. Therefore, we add  $\Delta R_{CNT}$  to the diagonal elements of the real part of the impedance matrix  $\mathbf{R}$  and we add  $\Delta\omega L_{CNT}$  to the diagonal elements of the imaginary part of the impedance matrix  $\mathbf{X}$ , where  $\Delta$  is the length of each segment. From our extensive study of the impedance matrices of different CNT shapes, we found that the real part of the impedance matrix  $\mathbf{R}$  is dominated by the  $\Delta R_{CNT}$  term. Therefore, the matrix  $\mathbf{R}$  is mostly a diagonal matrix with the diagonal elements more than  $10^6$  larger than any of the off-diagonal elements. A

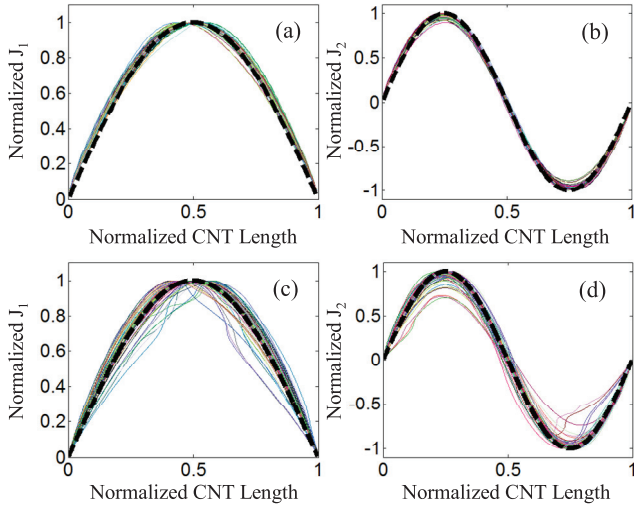


Fig. 12. Amplitude normalized eigencurrents or characteristic modes (a)  $J_1$  at the first resonance and (b)  $J_2$  at the second resonance for CNTs of contour length  $L = 193$  nm and persistence length  $P = 83$  nm and the normalized eigencurrents or characteristic modes (c)  $J_1$  at the first resonance and (d)  $J_2$  at the second resonance for CNTs of contour length  $L = 624$  nm and persistence length  $P = 83$  nm. In each subplot, the thin lines represent the exact eigencurrents calculated using (9) and the different colors correspond to different CNT shapes. The thick black dashed lines represent the approximation to the eigencurrents using (13).

similar observation was also stated by Sotiropoulos *et al.* [11, p. 113] in their analysis of scattering from arrays of straight CNTs. Therefore, we can approximate the normalization factor by assuming the relation

$$R_{ii} \approx \Delta R_{CNT} \quad \text{and} \quad R_{ij} \approx 0. \quad (14)$$

Also, at the resonances, the eigencurrents  $J_n$  can be approximated by (13). Therefore, at the  $n$ th resonances, the normalization factor  $\langle \mathbf{J}_n, \mathbf{R}\mathbf{J}_n \rangle$  can be approximated as

$$\langle \mathbf{J}_n, \mathbf{R}\mathbf{J}_n \rangle = \sum \mathbf{J}_n^T \cdot (\mathbf{R}\mathbf{J}_n) \quad (15a)$$

$$\langle \mathbf{J}_n, \mathbf{R}\mathbf{J}_n \rangle \approx \int_0^L \sin\left(\frac{n\pi\ell}{L}\right) R_{CNT} \sin\left(\frac{n\pi\ell}{L}\right) d\ell = \frac{LR_{CNT}}{2}. \quad (15b)$$

For the  $L = 193$  nm CNTs studied in this paper, the value of this normalization factor (which has units of power) corresponds to 106.9 W and is independent of CNT shape. Fig 13(a) shows this normalization factor for the 100 different CNTs shapes, with  $L = 193$  nm and  $P = 83$  nm, as calculated directly from the MOM  $\mathbf{R}$  matrix with no approximation. Fig. 13(a) shows that the normalization factor varies between  $(106.9 \pm 1)$  W justifying the approximation in (14) and (15). Also, all the normalization factors for the different eigencurrents at the different resonances have the same normalization value as predicted from (15) and shown in Fig. 13. This is in contrast with PEC wires where the normalization factor depends on both the shape and the eigencurrent. To demonstrate this dependence, Fig. 13(b) shows the normalization factors for the same shapes in (13a) but assuming that the CNTs are perfectly conducting. Also, the normalization factors

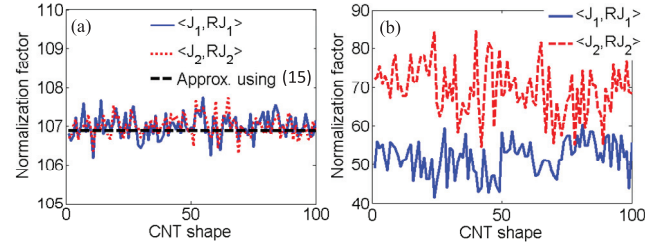


Fig. 13. Normalization factor for the first two eigencurrents for (a) CNTs with the Drude model conductivity and (b) PEC CNTs.

in Fig. 13(b) are calculated at frequencies where the perfectly conducting CNTs resonate, which are different from those in Fig. 13(a), where the CNTs have the Drude model conductivity (4). Fig. 13(b) clearly shows that the normalization factor for perfectly conducting wires at resonance depends on both the shape and the eigencurrent.

### C. Modal Excitation Coefficients $V_n$ for CNTs

In Fig. 11, the modal significance coefficients ( $MS_n$ ) were plotted versus frequency. At the  $m$ th resonance,  $MS_m$  is close to unity indicating that  $\lambda_m$  is close to zero. For  $n \neq m$ , the magnitude of  $\lambda_n$  is large and therefore the contribution from the other eigencurrents is negligible. Using this fact, the extinction coefficient at the  $m$ th resonance termed  $C_{ext}(m)$  can be approximated for CNTs as a function of a single mode or eigencurrent  $J_m$  as follows:

$$C_{ext}(m) = \frac{\eta}{|\mathbf{E}^i|^2} \frac{|V_m|^2}{\langle \mathbf{J}_m, \mathbf{R}\mathbf{J}_m \rangle}. \quad (16)$$

We will start with the MEC term  $V_m$  for simple shapes. The first case we consider will be a straight CNT aligned along the  $x$ -axis with a plane wave incident at an arbitrary angle  $\theta$  with the  $z$ -axis and an angle  $\varphi$  with the  $x$ -axis. The Transverse Magnetic (TM) polarization is employed. At the  $m$ th resonance, the free-space wavelength can be expressed as  $\lambda_0 = 2L/(m\alpha)$ . Therefore, the magnitude of the propagation constant  $k$  can be expressed as  $k = (m\pi\alpha)/L$ . The propagation factor at the  $m$ th resonance, the incident electric field, and the  $m$ th eigencurrent can be expressed as

$$\mathbf{k} = -\frac{m\pi\alpha}{L} (\sin(\theta) \cos(\varphi) \hat{\mathbf{a}}_x + \sin(\theta) \sin(\varphi) \hat{\mathbf{a}}_y + \cos(\theta) \hat{\mathbf{a}}_z) \quad (17)$$

$$\begin{aligned} \mathbf{E}^i &= \hat{\mathbf{a}}_E \exp(j\mathbf{k} \cdot \mathbf{r}) \\ &= [\cos(\theta) \cos(\varphi) \hat{\mathbf{a}}_x + \cos(\theta) \sin(\varphi) \hat{\mathbf{a}}_y \\ &\quad - \sin(\theta) \hat{\mathbf{a}}_z] \exp(j\mathbf{k} \cdot \mathbf{r}) \end{aligned} \quad (18)$$

$$\mathbf{J}_m = \sin(m\pi\ell) \hat{\mathbf{a}}_x \quad (19)$$

where  $\mathbf{r}$  is the position vector along the length of CNT and can be expressed for a straight CNT as:  $\mathbf{r} = \ell L \hat{\mathbf{a}}_x$  where  $\ell$  varies from 0 to 1. In (19), we have used the estimate for the magnitude of the eigencurrent in (13) and the eigencurrent is in the  $x$ -direction in this case because the wire is straight and oriented in the  $x$ -direction. The first MEC,  $V_1$ , can be estimated as

$$V_1 = \int_0^1 \mathbf{J}_1 \cdot \mathbf{E}^i dl \quad (20a)$$

$$V_1 = \int_0^1 \cos(\theta) \cos(\varphi) \sin(\pi \ell) \exp\left(j \frac{\pi \alpha}{L} \sin(\theta) \cos(\varphi) \ell L\right) dl \quad (20b)$$

$$|V_1| = \left(\frac{2L}{\pi}\right) \frac{\cos(\theta) \cos(\varphi) \cos[(\pi \alpha / 2) \sin(\theta) \cos(\varphi)]}{[1 - \alpha^2 \sin^2(\theta) \cos^2(\varphi)]}. \quad (20c)$$

Similarly, expressions can be derived for the magnitude of the second and third MEC. The previous expressions were found to match within 5% to those achieved using the exact eigencurrents as calculated by the MOM for a straight CNT.

The advantage of the closed-form expression in (20) is that it is general and can be applied to other straight nanowires besides CNTs. For example, the resonances in the total extinction coefficient of gold and silver nanowires have received significant experimental interest [45]–[47]. Moreover, the variation in the resonance with the relative angle between the incident wave and the axis of the gold nanowire has been measured for several resonances [45]–[47]. Equation (20) can be readily adapted to describe this variation by selecting the velocity factor  $\alpha$  for gold nanowires, which tends to be larger than the values for CNTs [45]–[47].

The velocity factor is directly dependent on the inductance  $L_{CNT}$  defined in (5). To account for possible variations in  $L_{CNT}$ , which will change the velocity factor  $\alpha$ , Fig. 14 shows the MEC for three velocity factors  $\alpha = 1, 0.5, 0.016$ . Fig. 14 shows the MEC for different incident directions  $\theta$  with respect to the  $z$ -axis and at  $\varphi = 0$  with the  $x$ -axis. The case where  $\alpha = 1$  represents the case of a perfect conductor,  $\alpha = 0.016$  is a typical CNT value, and  $\alpha = 0.5$  is an intermediate value that is similar to the velocity factors exhibited in some gold nanowires. Fig. 14(a) shows that  $|V_1|^2$  is weakly dependent on the velocity factor  $\alpha$ . The factor  $|V_1|^2$  is maximum at normal incidence to the CNT and minimum when the incident wave is propagating along the axis of the CNT for the TM polarization. Since the other factors in (9) and (10) do not depend on the excitation or electric field directions, this indicates that the peak amplitude of the first resonance is maximum at normal incidence and minimum when the incident wave is propagating along the axis of the CNT.

On the other hand, Fig. 14(b) and (c) shows that  $|V_2|^2$  and  $|V_3|^2$ , respectively, are strongly dependent on the velocity factor. The factor  $|V_2|^2$  is minimal at both  $\theta = 0^\circ$  and  $\theta = 90^\circ$  and decreases with the velocity factor  $\alpha$  for all  $\theta$  values. This indicates that a second resonance can only be obtained at oblique incidence for a straight CNT and only if it has a large velocity factor  $\alpha$ . However, typical velocity factors for a CNT are between 0.01 and 0.02, which will cause  $|V_2|^2$  to converge to negligible values at all angles of incidence. This indicates that there is no excitation direction that can generate a second resonance for a perfectly straight CNT. Moreover, the results in Fig. 4(b) help explain the trend in Fig. 8 which studied

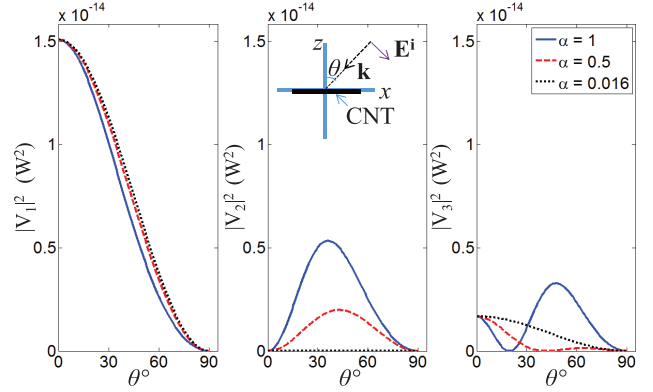


Fig. 14. Variation in the (a) first MEC, (b) second MEC, and (c) third MEC with the incident direction  $\theta$  and value of the velocity factor  $\alpha$  for a straight CNT. The inset shows the straight CNT, the incident plane wave, and the electric field directions.

worm-like CNTs of different persistence lengths. The reported results showed that the average peak amplitude of the second resonance decreased as the persistence length  $P$  increased for the  $x$ -polarization. This decrease occurs because as the persistence length increases the CNTs become straighter and from Fig. 14(b) a perfectly straight CNT cannot exhibit a second resonance for any  $\mathbf{E}^i$  direction or CNT orientation.

An interesting observation in (17)–(20) is that when the velocity factor is in the range suitable for CNTs,  $\alpha = 0.01$  to  $0.02$ , the magnitude of the propagation constant  $k = (m\pi\alpha)/L$  is very small for the first few resonances. Therefore, the electric field over the length of the CNT as in (10b) can be approximated as

$$\mathbf{E}^i = \hat{\mathbf{a}}_E \exp(j\mathbf{k} \cdot \mathbf{r}) \approx \hat{\mathbf{a}}_E(1) \approx \hat{\mathbf{a}}_E \quad (21)$$

where  $\hat{\mathbf{a}}_E$  is the unit vector in the direction of the incident electric field. This will significantly simplify the calculation of the MEC and will also simplify the relationship between the shape of the CNT and the peak amplitude of each resonance. It will become much easier, just from the knowledge of the CNT shape, to identify whether it will exhibit a large or a small  $m$ th resonance.

For example, consider the following three simple shapes in Fig. 15. In Fig. 15, the top view of the shapes is shown (i.e., looking down in the  $-z$  direction). In all cases, the incident wave is propagating in the negative  $z$ -direction and the electric field is polarized in the  $x$ -direction. The direction of the incident electric field is shown as the solid arrow. Fig. 15(a)–(c) shows the first eigencurrent  $\mathbf{J}_1$  at the first resonance and Fig. 15(d)–(f) shows the second eigencurrent  $\mathbf{J}_2$  at the second resonance. In Fig. 15(a)–(c), the eigencurrent has only a single maximum at the center of the wire. The direction and position of this maximum is shown as a dashed arrow. Fig. 15(a) shows that for a straight CNT, the current and the electric field are in the same direction all over the length of the CNT. The dot product between the first eigencurrent and the electric field will then be nonzero all over the CNT causing the integral in (10b) to have a large value. Therefore,  $V_1$  will be large and since the peak amplitude at the first resonance is proportional to  $|V_1|^2$ ,

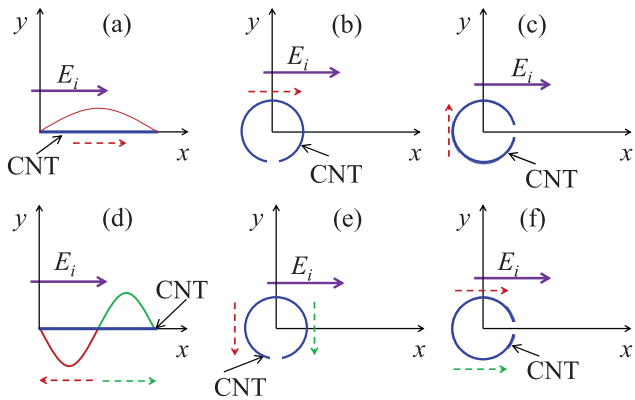


Fig. 15. Three sketches showing the first eigencurrent at the first resonance for (a) straight CNT, (b) C-shaped CNT rotated  $90^\circ$ , and (c) C-Shaped CNT and three sketches showing the second eigencurrent at the second resonance for (d) straight CNT, (e) C-shaped CNT rotated  $90^\circ$ , and (f) C-Shaped CNT.

a large first resonance will be exhibited for the straight CNT in Fig. 15(a). In Fig. 15(b), a C-shaped CNT rotated  $90^\circ$  is oriented such that at the middle of the CNT, where  $J_1$  is maximum, the current is in the same direction as the incident field. Therefore, the dot product between the incident field and  $J_1$  will be nonzero leading to a relatively large  $V_1$  in (10b) and therefore a large first resonance. In Fig. 15(c), for a C-shaped CNT, the direction of the current at the maximum is perpendicular to the incident electric field. Therefore, the dot product in (10b) will be small leading to a small value of  $V_1$ , which indicates a small first resonance peak amplitude.

To study the second resonance for the shapes in Fig. 15(d)–(f), we now switch to the second eigencurrent  $J_2$ . The second eigencurrent has two maxima: one negative and one positive as shown in Fig. 12(b). The location of the negative maximum (red) is approximately at a quarter of the CNT length and the positive maximum (green) is approximately at three quarters of the CNT length as indicated in Fig. 15(d)–(f). For the straight CNT in Fig. 15(d), the eigencurrent  $J_2$  is in the same direction as the incident field. However, over the first half of the CNT  $J_2$  is negative and over the other half it is positive. Therefore, when the dot product between the incident electric field and  $J_2$  is summed up in the integration in (10b), the positive and negative values cancel and the result is close to zero leading to a small  $V_2$  and a small second resonance. In Fig. 15(e), the positive and negative maximum of  $J_2$  occur at locations where the CNT is oriented in the  $y$ -direction. Therefore, the maxima of  $J_2$  are perpendicular to the incident field leading to a small dot product. Therefore,  $V_2$  is small and a small second resonance is achieved for the  $90^\circ$  rotated C-shaped CNT in Fig. 15(e). Finally, in Fig. 15(f), the C-shaped CNT is oriented such that the two maxima of the current now point in the same direction, which is the positive  $x$ -direction. Therefore, the dot product between the incident electric field and  $J_2$  will be positive over the whole length of the CNT leading to a large  $V_2$  and a large second resonance. These qualitative observations based on Fig. 15 explain the resonances, as calculated using the MOM exhibited in Fig. 4.

Similar observations of the second resonance were reported for individual short silver nanowires using time-dependent density functional theory (TDDFT) calculations [48], [49]. For straight silver wires, no second resonance was observed. As the silver wires became more curved, the second resonance emerged [48], [49]. This behavior of the second resonance, calculated using the quantum TDDFT in [48] and [49], agrees with our continuum TCM predictions in Fig. 15 which provides further validity to our results. However, experimental detection of the second resonance from nonstraight CNTs is still pending.

Most of the THz measurements on CNT samples involved multiple interacting tubes. The interaction between the CNTs can typically lead to additional resonances that can overlap with the second resonance predicted by our result. Nevertheless, the second resonance can be used to provide different theoretical interpretations to experimental results. For example, in the paper of Bommeli *et al.*, experimental measurements of the effective conductivity of a CNT film showed a resonance in the THz range when the electric field was parallel to the tubes [50]. When the electric field was perpendicular to the tubes, a resonance was also exhibited in the effective conductivity of the CNT film, but it occurred at a slightly higher frequency than the resonance exhibited when the field was parallel to the tubes [50]. We hypothesize that this shift to higher frequency can be explained by our results in Figs. 8 and 10. These figures show that when the incident field is perpendicular to the major axis of the tube, the first resonance vanishes and the response is mainly due to the second resonance. Since the second resonance always occurs at a higher frequency than the first resonance, we hypothesize that this can be one of the factors that can explain why the resonance in the effective conductivity of the CNT film shifted to a higher frequency when the field was perpendicular to the tubes as presented by Bommeli *et al.* [50].

Another set of interesting CNT shapes is shown in Fig. 16. In Fig. 16(a)–(e), all the CNTs are arc-shaped with the same radius of curvature and, therefore, they have the same persistence length. Fig. 16(f) shows the peak amplitude of the first resonance calculated from the CNT arcs in Fig. 16(a)–(e). In Fig. 16, the incident electric field is always in the  $x$ -direction and therefore we are only concerned with the  $x$ -component of the first eigencurrent at the first resonance  $J_1$  to explain the variations in the peak amplitude of the first resonance. Fig. 16(f) shows that the peak amplitude of the first resonance increases until  $L = 384$  nm. Beyond this length, the peak amplitude of the first resonance decreases similar to the trend in Fig. 10 which considered worm-like CNTs with the same contour lengths values as in Fig. 16. To explain this trend, it is important to note that the amplitude of  $J_1$  is positive over the length of the CNT as shown in (13) and in Fig. 12. This means that it will be pointing from one end of the CNT to the other end all over its length. However, depending on the orientation of each CNT segment, the  $x$ -component of  $J_1$  can be directed toward the positive  $x$  direction, indicated with a green (+) symbol in Fig. 16, or toward the negative  $x$  direction, indicated with a red (–) symbol in Fig. 16.

In Figs. 16(a)–(c), the  $x$ -component of  $J_1$  is positive over the entire length of the CNT and the longer the CNT, the larger

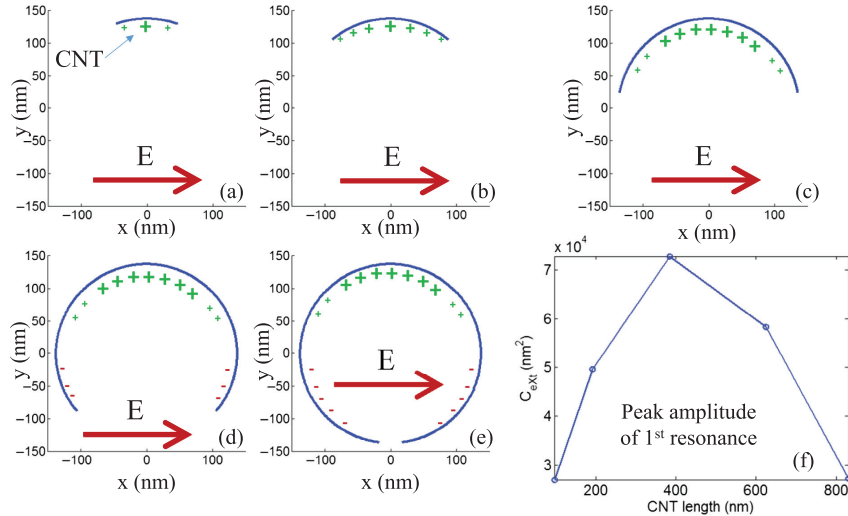


Fig. 16. Sketches showing the first eigencurrent at the first resonance for arc-shaped CNTs with contour lengths: (a)  $L = 96$  nm; (b) 193 nm; (c) 384 nm; (d) 624 nm; and (e) 831 nm. The corresponding peak amplitudes of the first resonance for the previously mentioned arcs are shown in (f). All the arc-shaped CNTs have the same radius of curvature. The CNT locations where the  $x$ -component of the first eigencurrent is pointing toward the positive  $x$ -direction are indicated with a green (+) symbol, whereas the locations where the  $x$ -component of the first eigencurrent is pointing toward the negative  $x$  direction are indicated with a red (-) symbol. The size of the (+) and (-) symbols roughly correspond to the magnitude of the first eigencurrent.

is the MEC  $V_1$  as given in (10b). As the length of the CNT arc increases to  $L = 624$  nm and  $L = 831$  nm, the curvature in the CNT arc causes the  $x$ -component of the vector  $\mathbf{J}_1$  to be directed toward the negative  $x$ -direction over some segments of the CNT. Therefore, the dot product between the incident field and the first eigencurrent in (10b) will be positive in some regions and negative in others, and the peak amplitude of the first resonance starts to decrease. It is also important to note that the normalization factor  $\langle \mathbf{J}_n, \mathbf{R}\mathbf{J}_n \rangle$  increases monotonically with the CNT length. However, the peak amplitude of the first resonance is proportional to the square of the magnitude of  $V_1$  and only inversely proportional to the normalization factor  $\langle \mathbf{J}_n, \mathbf{R}\mathbf{J}_n \rangle$  as shown in (15). Therefore, the trend of that the peak amplitude of the first resonance follows is more sensitive to the variations in  $V_1$ .

## V. SIMPLIFIED FORMULATIONS CONNECTING THE SHAPE OF THE CNTS WITH THE PEAKS AMPLITUDE OF THE RESONANCES

The previous sections primarily presented four approximations to simplify the rigorous TCM analysis of CNTs. In the following section, we will demonstrate that these approximations are applicable for a wide variety of CNT shapes with different contour and persistence lengths. The first approximation is that at the resonances, the current can be expressed only in terms of a single mode as indicated by the modal significance analysis in Section III-A. In the second approximation, the characteristic current can be approximated by the sinusoidal expression in (13). The third approximation is that the TCM normalization factor  $\langle \mathbf{J}_n, \mathbf{R}\mathbf{J}_n \rangle$  can be expressed as a function of the length of the CNT and its distributed resistance and that it is independent of the CNT shape and the mode as shown in (15). Finally, the phase variations of the incident electric field over the length of the CNT are neglected in the calculation

of the Modal Excitation Coefficient since the CNTs resonate at wavelengths much larger than their contour lengths. Using these four approximations, the relationship between the peak amplitude of the  $m$ th resonance and the shape of the CNT can be approximated as follows:

$$C_{ext}(m) \approx \frac{\eta}{(LR_{CNT}/2)} \left| \int_0^1 \sin(m\pi\ell) (\hat{\mathbf{t}}(\ell) \cdot \hat{\mathbf{a}}_{\mathbf{E}}) d\ell \right|^2 \quad (22)$$

where  $\hat{\mathbf{t}}(\ell)$  is the unit vector tangent to the wire at point  $\ell$  and  $\hat{\mathbf{a}}_{\mathbf{E}}$  is the unit vector in the direction of the incident electric field. Equation (22) assumes that the incident field has a magnitude of unity. If it is different from unity, then the term  $|\mathbf{E}^i|^2$  needs to be added to the denominator in (22).

To test the validity of the above relations, Figs. 17 and 18 compare the peak amplitude of the first resonance as calculated by the MOM and as calculated by the approximate relationship in (22) for a wide variety of shapes. All the CNTs in Figs. 17 and 18 are aligned parallel to the  $x$ -axis, following the methodology described in Fig. 6, and the incident wave is propagating in the negative  $z$ -direction and the electric field is polarized in the  $x$ -direction. Fig. 17(a)–(d) shows the peak amplitude of the first resonance for  $P = 8.7$  nm,  $P = 35$  nm,  $P = 83$  nm, and  $P = 153$  nm, respectively. The CNTs in Fig. 17 have the same contour length,  $L = 193$  nm. Fig. 18(a)–(e) shows exactly the same information as Fig. 17 but for  $L = 96$  nm,  $L = 193$  nm,  $L = 384$  nm,  $L = 624$  nm, and  $L = 831$  nm, respectively. All the shapes in Fig. 18 have the same persistence length  $P = 83$  nm. We see close agreement between the full-wave peak amplitudes calculated using the MOM in Figs. 17 and 18 and the peak amplitudes calculated using the approximate TCM relations in (22). The advantage of the approximate TCM relations is that they are simple geometrical factors, much simpler than the MOM full-wave calculation,

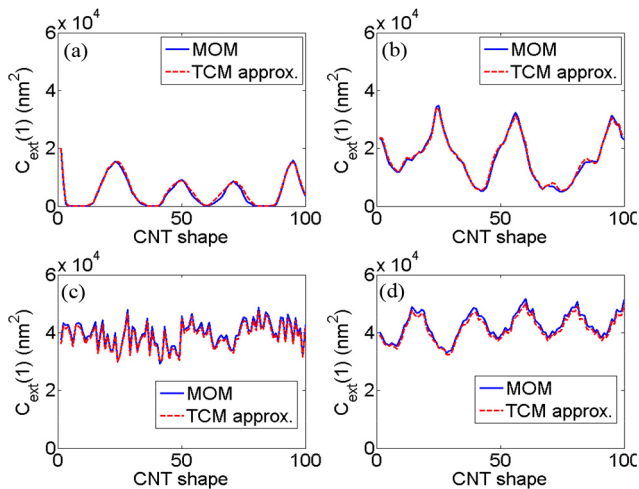


Fig. 17. Peak amplitude of the first resonance calculated using the TCM approximation and the MOM when the incident electric field is polarized in the  $x$ -direction for CNTs with contour length  $L = 193$  nm and persistence lengths (a)  $P = 8.7$  nm, (b)  $P = 8.7$  nm, (c)  $P = 83$  nm, and (d)  $P = 153$  nm.

and they only require the knowledge of the CNT shape and the direction of the incident electric field. Therefore, the approximate TCM relations help elucidate the relation between the shape of the CNT and the peak amplitude of the resonance at a significantly lower computational cost than full-wave electromagnetic simulations. The other resonances and polarizations, not illustrated in Figs. 17 and 18 due to space limitations, show similar agreement between the MOM and the TCM approximation in (22).

However, for the shortest persistence length, Fig. 17(a), and the two largest contour lengths considered,  $L = 624$  nm in Fig. 18(d) and  $L = 831$  nm in Fig. 18(e), some shapes show non-negligible differences between the peak amplitude calculated using the MOM calculation and the TCM approximation in (22). We studied these cases thoroughly to understand which of the four approximations used to derive (22) is responsible for this difference. We found that for the highly twisted CNT shapes, the eigencurrents are considerably different from the approximation in (13) as shown in Fig. 12(c) and (d). Therefore, the calculation of the MEC in (10b),  $V_n$ , will be relatively different from the exact values. The normalization factors  $\langle \mathbf{J}_n, \mathbf{R}\mathbf{J}_n \rangle$  are also function of the eigencurrents. Therefore, the deviation of the exact eigencurrents from the expression in (13) also causes the exact normalization factors  $\langle \mathbf{J}_n, \mathbf{R}\mathbf{J}_n \rangle$  to deviate from the approximation in (15).

The other two approximations used to derive (22), which are that the current at the resonances can be expressed only in terms of a single mode and that the phase variations of the incident electric field can be neglected as in (22), are still valid. If longer or more twisted CNTs than those employed in this work are considered, then the eigencurrent approximation in (13) will start to significantly diverge from the true eigencurrents and the approximation in (22) needs to be amended. As a rule of thumb, if  $L/P < 10$ , the TCM approximation in (22) shows close agreement with the MOM values. The majority of the shapes considered in this work satisfy this condition and, therefore, the approximation in (22) is still valid as shown in Figs. 17 and 18.

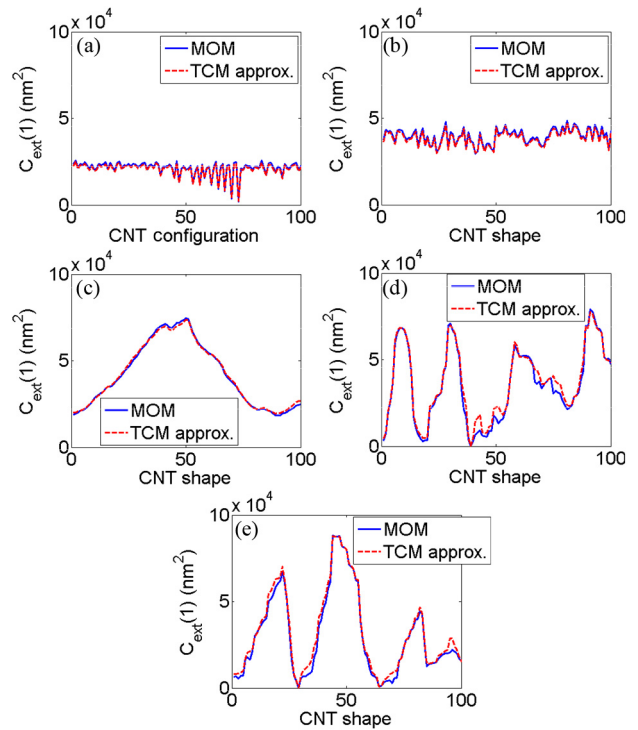


Fig. 18. Peak amplitude of the first resonance calculated using the TCM approximation and the MOM when the incident electric field is polarized in the  $x$ -direction for CNTs with persistence length  $P = 83$  nm and contour lengths (a)  $L = 96$  nm, (b)  $L = 193$  nm, (c)  $L = 384$  nm, (d)  $L = 624$  nm, and (e)  $L = 831$  nm.

Finally, the range of applicability of the approximation in (22) depends also on the model and parameters used to describe the conductivity of the CNT. If alternative models or parameters are used, the range of validity of the approximation in (22) might vary. This will be the focus of future work. However, the main contribution of this work is 1) to show that the shape of CNTs has a strong effect on their electromagnetic scattering characteristics and 2) that the exact TCM in (9) and (10) can be used to efficiently explain this shape dependence. Some or all of the various approximations may break down, but these two observations are expected to remain valid regardless of the conductivity model or parameters used to describe the conductivity of the CNTs.

## VI. CONCLUSION AND FUTURE WORK

Using the MOM formulation for ATW, we have calculated the total extinction coefficient spectrum of hundreds of different CNT shapes with different contour and persistence lengths. The calculations have shown that CNTs with different shapes exhibit a wide variability in the peak amplitudes of the resonances in the total extinction coefficient spectrum even if they have the same contour and persistence lengths. Therefore, the shape of CNTs has to be taken into consideration when designing composites for electromagnetic applications. To explain this shape dependence, we performed rigorous analysis of the electric current distributions on CNTs using the TCM. We developed approximate formulations that directly link the CNT

shape with the peak amplitudes of the resonances. These formulations can be used to facilitate the design of novel CNT devices and systems. In future work, the scattering characteristics of multiple CNTs will be investigated using a dual MOM and TCM approach similar to the one evoked in this paper for an individual CNT. Finally, we will also explore, using the formulas in (22), the design of optimized CNT devices by varying the shapes of the CNTs to meet desired requirements.

## REFERENCES

- [1] M. Zhang and J. Li, "Carbon nanotube in different shapes," *Mater. Today*, vol. 12, no. 6, pp. 12–18, 2009.
- [2] F. T. Fisher, R. D. Bradshaw, and L. C. Brinson, "Fiber waviness in nanotube-reinforced polymer composites-I: Modulus predictions using effective nanotube properties," *Compos. Sci. Technol.*, vol. 63, pp. 1705–1722, 2003.
- [3] C. Li, E. Thostenson, and T. Chou, "Effect of nanotube waviness on the electrical conductivity of carbon nanotube-based composites," *Compos. Sci. Technol.*, vol. 68, pp. 1445–1452, 2008.
- [4] F. Deng, Q. Zheng, L. Wang, and C. Nan, "Effects of anisotropy, aspect ratio, and nonstraightness of carbon nanotubes on thermal conductivity of carbon nanotube composites," *Appl. Phys. Lett.*, vol. 90, p. 021914, 2007.
- [5] F. Vargas-Lara, A. Hassan, E. Garboczi, and J. Douglas, "Intrinsic conductivity of carbon nanotubes and graphene sheets having a realistic geometry," *J. Chem. Phys.*, vol. 143, pp. 204902-1–204902-16, 2015.
- [6] G. Miano and F. Villone, "An integral formulation for the electrodynamic of metallic carbon nanotubes based on a fluid model," *IEEE Trans. Antennas Propag.*, vol. 54, no. 10, pp. 2713–2724, Oct. 2006.
- [7] G. Hanson, "Fundamental transmitting properties of carbon nanotube antennas," *IEEE Trans. Antennas Propag.*, vol. 53, no. 11, pp. 3426–3435, Nov. 2005.
- [8] P. Burke, S. Li, and Z. Yu, "Quantitative theory of nanowire and nanotube antenna performance," *IEEE Trans. Nanotechnol.*, vol. 5, no. 4, pp. 314–334, Jul. 2006.
- [9] G. Slepuyan, M. Shuba, S. Maksimenko, and A. Lakhtakia, "Theory of optical scattering by achiral carbon nanotubes and their potential as optical nanoantennas," *Phys. Rev. B*, vol. 73, p. 195416, 2006.
- [10] J. Hao and G. Hanson, "Electromagnetic scattering from finite-length metallic carbon nanotubes in the lower IR bands," *Phys. Rev. B*, vol. 74, p. 035119, 2006.
- [11] A. Sotiropoulos, I. Plegas, S. Koulouridis, and H. Anastassiou, "Scattering properties of carbon nanotube arrays," *IEEE Trans. Electromagn. Compat.*, vol. 54, no. 1, pp. 110–117, Feb. 2012.
- [12] G. Slepuyan, M. Shuba, S. Maksimenko, C. Thomsen, and A. Lakhtakia, "Terahertz conductivity peak in composite materials containing carbon nanotubes: Theory and interpretation of experiment," *Phys. Rev. B*, vol. 81, p. 205423, 2010.
- [13] M. Shuba *et al.*, "Experimental evidence of localized plasmon resonance in composite materials containing single-wall carbon nanotubes," *Phys. Rev. B*, vol. 85, p. 165435, 2012.
- [14] M. Shuba, A. Melnikov, A. Paddubskaya, P. Kuzhir, and S. Maksimenko, "Role of finite-size effects in the microwave and subterahertz electromagnetic response of a multiwall carbon-nanotube-based composite: Theory and interpretation of experiments" *Physical Review B*, vol. 88, p. 045436, 2013.
- [15] Q. Zhang *et al.*, "Plasmonic nature of the terahertz conductivity peak in single-wall carbon nanotubes," *Nano Lett.*, vol. 13, no. 12, pp. 5991–5996, 2013.
- [16] A. Hassan and E. Garboczi, "Electromagnetic scattering from randomly-centered parallel single-walled carbon nanotubes embedded in a dielectric slab," *IEEE Trans. Antennas Propag.*, vol. 62, no. 10, pp. 5230–5241, Oct. 2014.
- [17] W. C. Gibson, *The Method of Moments in Electromagnetics*. London, U.K.: Chapman & Hall/CRC Press, 2008.
- [18] R. Garbacz, "Modal expansions for resonance scattering phenomena," *Proc. IEEE*, vol. 53, no. 8, pp. 856–864, Aug. 1965.
- [19] R. Harrington and J. Mautz, "Theory of characteristic modes for conducting bodies," *IEEE Trans. Antennas Propag.*, vol. 19, no. 5, pp. 622–628, Sep. 1971.
- [20] R. Harrington and J. Mautz, "Computation of characteristic modes for conducting bodies," *IEEE Trans. Antennas Propag.*, vol. 19, no. 5, pp. 629–639, Sep. 1971.
- [21] R. Harrington, J. Mautz, and Y. Chang, "Characteristic modes for dielectric and magnetic bodies," *IEEE Trans. Antennas Propag.*, vol. 20, no. 2, pp. 194–198, Mar. 1972.
- [22] Q. Wu and D. Su, "A broadband model of the characteristic currents for rectangular plates," *IEEE Trans. Electromagn. Compat.*, vol. 55, no. 4, pp. 725–732, Aug. 2013.
- [23] M. Cabedo-Fabres, E. Antonino-Daviu, A. Valero-Nogueira, and M. Bataller, "The theory of characteristic modes revisited: A contribution to the design of antennas for modern applications," *IEEE Antennas Propag. Mag.*, vol. 49, no. 10, pp. 52–68, Oct. 2007.
- [24] H. Li, Z. Miers, and B. K. Lau, "Design of orthogonal MIMO handset antennas based on characteristic mode manipulation at frequency bands below 1 GHz," *IEEE Trans. Antennas Propag.*, vol. 62, no. 5, pp. 2756–2766, May 2014.
- [25] S. Wang and H. Arai, "Analysis of an optimized notch array antenna by using the theory of characteristic modes," *IEEE Antennas Wireless Propag. Lett.*, vol. 13, pp. 253–256, Feb. 12, 2014.
- [26] B. Raines and R. Rojas, "Wideband characteristic mode tracking," *IEEE Trans. Antennas Propag.*, vol. 60, no. 7, pp. 3537–3541, Jul. 2012.
- [27] Q. Wu, S. Guo, and D. Su, "On the eigenmodes of small conducting objects," *IEEE Antennas Wireless Propag. Lett.*, vol. 13, pp. 1667–1670, Aug. 2014.
- [28] B. Natarajan *et al.*, "The evolution of carbon nanotube network structure in unidirectional nanocomposites resolved by quantitative 3D electron tomography," *ACS Nano*, vol. 9, pp. 6050–6058, 2015.
- [29] K. Kremer and G. Grest, "Dynamics of entangled linear polymer melts: A molecular dynamics simulation," *J. Chem. Phys.*, vol. 92, p. 5057, 1990.
- [30] D. Frenkel and B. Smit, *Understanding Molecular Simulations*. San Diego, CA, USA: Academic, 2002.
- [31] H. Lee *et al.*, "Percolation of two-dimensional multiwall carbon nanotube networks," *Appl. Phys. Lett.*, vol. 95, p. 134104, 2009.
- [32] H. Lee, C. Yun, H. Kim, and C. Lee, "Persistence Length of multi-walled carbon nanotubes with static bending," *J. Phys. Chem. C*, vol. 111, pp. 18882–18887, 2007.
- [33] Nanointegris. (2016, Feb.) [Online]. Available: <http://www.nanointegris.com/en/metallic>
- [34] "Reference material 8281 single-wall carbon nanotubes (dispersed, three length-resolved populations)," NIST Reference Material, 2013 [Online]. Available: [https://www-s.nist.gov/srmors/view\\_report.cfm?srm=8281](https://www-s.nist.gov/srmors/view_report.cfm?srm=8281)
- [35] F. Vargas-Lara and J. Douglas, "Confronting the complexity of CNT materials," *Soft Matter*, vol. 11, pp. 4888–4898, 2015.
- [36] X. Lia, W. Lehmana, and S. Fischer, "The relationship between curvature, flexibility and persistence length in the tropomyosin coiled-coil," *J. Struct. Biol.*, vol. 170, no. 2, pp. 313–318, 2010.
- [37] D. Miron, *Small Antenna Design (Communications Engineering Series)*. Burlington, MA, USA: Newnes, 2006.
- [38] G. Slepuyan, S. Maksimenko, A. Lakhtakia, O. Yevtushenko, and A. V. Gusakov, "Electrodynamics of carbon nanotubes: Dynamic conductivity, impedance boundary conditions, surface wave propagation," *Phys. Rev. B*, vol. 60, p. 17136, 1999.
- [39] G. Hanson, "Radiation efficiency of nano-radius dipole antennas in the microwave and far-infrared regimes," *IEEE Antennas Propag. Mag.*, vol. 50, no. 3, pp. 66–77, Jun. 2008.
- [40] L. Liu, C. Jayanthi, and S. Wu, "Structural and electronic properties of a carbon nanotorus: Effects of delocalized and localized deformations," *Phys. Rev. B*, vol. 64, p. 033412, 2001.
- [41] A. Polimeridis, M. Reid, S. Johnson, J. White, and A. Rodriguez, "On the computation of power in volume integral equation formulations," *IEEE Trans. Antennas Propag.*, vol. 63, no. 2, pp. 611–620, Feb. 2015.
- [42] J. Kraus, *Antennas*, 1st ed. New York, NY, USA: McGraw-Hill, 1950.
- [43] S. Alyones and C. W. Bruce, "Curved fiber scattering," *Prog. Electromagn. Res. M*, vol. 17, pp. 225–236, 2011.
- [44] H. Arkin and W. Janke, "Gyration tensor based analysis of the shapes of polymer chains in an attractive spherical cage," *J. Chem. Phys.*, vol. 138, p. 054904, 2013.
- [45] G. Schider *et al.*, "Plasmon dispersion relation of Au and Ag nanowires," *Phys. Rev. B*, vol. 68, p. 155427, 2003.
- [46] E. Payne, K. Shuford, S. Park, G. Schatz, and C. Mirkin, "Multipole plasmon resonances in gold nanorods," *J. Phys. Chem. B*, vol. 110, pp. 2150–2154, 2006.
- [47] J. Dorfmueller, R. Vogelgesang, W. Khunsin, C. Rockstuhl, C. Etrich, and K. Kern, "Plasmonic nanowire antennas: Experiment, simulation, and theory," *Nano Lett.*, vol. 10, pp. 3596–3603, 2010.
- [48] N. Karimova and C. Aikens, "Time-dependent density functional theory investigation of the electronic structure and chiroptical properties of curved and helical silver nanowires," *J. Phys. Chem. A*, vol. 119, pp. 8163–8173, 2015.

- [49] S. Swasey *et al.*, "Chiral electronic transitions in fluorescent silver clusters stabilized by DNA," *ACS Nano*, vol. 8, pp. 6883–92, 2014.
- [50] F. Bommeli *et al.*, "Evidence of anisotropic metallic behaviour in the optical properties of carbon nanotubes," *Solid-State Commun.*, vol. 99, no. 7, pp. 513–517, 1996.



**Ahmed M. Hassan** (S'07–M'12) received the B.Sc. (with highest honors) and M.Sc. degrees in electronics and communications engineering from Cairo University, Giza, Egypt, in 2004 and 2006, respectively, and the Ph.D. degree in electrical engineering from the University of Arkansas, Fayetteville, AR, USA, in 2010.

From 2011 to 2012, he was a Postdoctoral Researcher with the Department of Electrical Engineering, University of Arkansas. From 2012 to 2015, he was a Postdoctoral Researcher with the

National Institute of Standards and Technology, Gaithersburg, MD, USA. Currently, he is an Assistant Professor with the Department of Computer Science Electrical Engineering, University of Missouri-Kansas City, Kansas City, MO, USA. His research interests include nanoelectromagnetics, bioelectromagnetics, nondestructive evaluation, experimental microwave, and terahertz imaging.

Dr. Hassan was the recipient of the Doctoral Academy Fellowship at the University of Arkansas and the Outstanding Poster Award in the 2014 21st Annual NIST Sigma Xi Postdoctoral Poster Presentation.



**Fernando Vargas-Lara** received the B.S. degree in physics from the National Polytechnic School, Quito, Ecuador, in 2003, and the Ph.D. degree in physics from Wesleyan University, Middletown, CT, USA, in 2013.

Since 2013, he has been a Postdoctoral Researcher with the Materials Science and Engineering Division, National Institute of Standards and Technology (NIST), Gaithersburg, MD, USA. His research interests include the study of the self-assembly of DNA-based structures, the transport and structural prop-

erties of polymers and complex shaped particles, and the electromagnetic properties of carbon nanotube and graphene composites.

Dr. Vargas-Lara is currently a member of the American Physics Society and American Chemistry Society. He was the recipient of the Material Measurement Laboratory Distinguished Associate Award at NIST in 2015 and the Soft Matter Poster Prize at the Boulder Summer School: Polymers in Soft and Biological Matter, University of Colorado Boulder, Boulder, CO, USA, in 2012.



**Jack F. Douglas** received the B.Sc. degree in chemistry and the M.S. degree in mathematics from Virginia Commonwealth University (VCU), Richmond, VA, USA, in 1979 and 1981, respectively, and the Ph.D. degree in chemistry from the University of Chicago, Chicago, IL, USA, in 1986.

During graduate school, he was an IBM Graduate Fellow (1985–1986). After receiving his doctorate, he was first a NATO Fellow with the Cavendish Laboratory, University of Cambridge, Cambridge, U.K., under the direction of Prof. Sam Edwards and

afterwards a National Research Council Postdoctoral Fellow with the National Institute of Standards and Technology (NIST), Gaithersburg, MD, USA. He then became a Research Scientist with the Polymers Division, NIST, until he was promoted to the position of NIST Fellow, the most Senior Scientific Position with NIST. He has authored approximately 400 papers covering a broad range of topics in statistical physics (transport properties of suspensions, percolation theory, random and self-avoiding walks, random surfaces, protein dynamics, the physics of worm-like polymers such as DNA, phase separation in polymer blends and solutions, self-assembly of block copolymers, polymer nanocomposites, rubber elasticity, self-assembly and molecular binding, crystallization under far from equilibrium conditions, the dynamics of grain boundaries, the dynamics of nanoparticles and thin films, photopolymerization, renormalization group theory, path-integration, and fractional calculus, surface interacting polymers, dewetting of polymer films, supercooled liquids and glasses, and entanglement interactions in polymer fluids).

Dr. Douglas' awards and recognition, apart from the fellowships mentioned above, include APS Fellow, Bronze Medal-Department of Commerce, 5-year rotation as an Editorial Board Member of *Physical Review Letters*, and he was selected for Phi Kappa Phi and Sigma Xi, and for the American Chemical Society Senior Award at VCU.



**Edward J. Garboczi** received the B.S. degree in physics (with highest honors) and the Ph.D. degree in condensed matter physics (theory) from Michigan State University, East Lansing, MI, USA, in 1980 and 1985, respectively.

From 1985 to 1988, he was a Research Physicist with Armstrong World Industries, Inc., Lancaster, PA, USA. From 1988 to 2014, he was a Physicist, Group Leader, and finally a Fellow with the Materials and Structural Systems Division, National Institute of Standards and Technology (NIST), Gaithersburg,

MD, USA. In 2014, he moved to the Division of Applied Chemicals and Materials Division, NIST, Boulder, CO, USA. His research interests include computational materials science, porous materials, electrical properties of nanocomposites, and 3-D particle shape analysis of a wide range of particles including gravel, sand, cement, chemical explosives, lunar soil, and metal powder for additive manufacturing.

Dr. Garboczi is a Fellow of the American Concrete Institute (ACI) and the American Ceramic Society (ACerS). He was the recipient of the ACI Robert E. Philleo Award, the ACerS Della Roy Lecture Award, the ACers Edward C. Henry Best Paper Award (Electronics Division), and a Silver Medal from the Department of Commerce for the creation of the Virtual Cement and Concrete Testing Laboratory.